ACS SENSORS

pubs.acs.org/acssensors
Article

Sensitivity Enhancement of CO_2 Sensors at Room Temperature Based on the CZO Nanorod Architecture

Baktiyar Soltabayev,* Yessimzhan Raiymbekov, Aidarbek Nuftolla, Amanzhol Turlybekuly, Gani Yergaliuly, and Almagul Mentbayeva*

Cite This: *ACS Sens.* 2024, 9, 1227−1238
Read Online

ABSTRACT: Cobalt-doped ZnO (CZO) thin films were deposited on glass substrates at room temperature by radio frequency (RF) magnetron sputtering of a single target prepared with ZnO and Co_3O_4 powders. Changes in the crystallinity, morphology, optical properties, and chemical composition of the CZO thin films were investigated at various sputtering powers of 45, 60, and 75 W. All samples presented a hexagonal wurtzite-type structure with a preferential *c*-axis at the (002) plane, along with a distinct change in the strain values through X-ray diffraction patterns. Scanning electron and atomic force microscopy revealed uniform and dense deposition of nanorod CZO samples with a high surface roughness (RMS). The Hall mobility and carrier concentration increased with the introduction of Co^+ ions into the ZnO matrix, as seen from the Hall effect study. The gradual increase of the power applied on the target source significantly affected the morphology of the CZO thin film, which is reflected in the CO_2-sensing performance. The best gas response to CO_2 was recorded for CZO-60 W with a response of 1.45 for 500 ppm CO_2, and the response/recovery times were 72 and 35 s, respectively. The distinguishing feature of the CZO sensor is its ability to effectively and rapidly detect the CO_2 target gas at room temperature (~27 °C, RT).

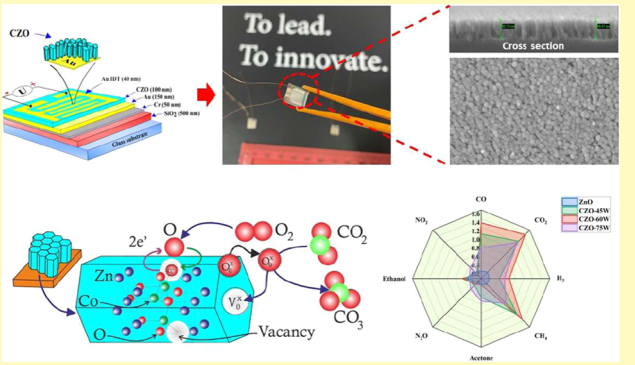

KEYWORDS: *CO_2 sensors, CZO nanorods, cobalt-doped ZnO, RF magnetron sputtering, room-temperature sensing, gas response, morphology control, thin film deposition*

In the last decades, many investigations have been devoted to hazardous gas detection technology in order to sustain its wide usage in various fields, such as healthcare, industrial safety, and environmental monitoring.[1,2] Within the functioning principles, different types of gas detection technology based on chemo-resistive, surface acoustic wave, optical, gas chromatography, and electrochemical sensors have been explored.[3,4] Among these detectors, chemo-resistive-type gas sensors based on metal oxide semiconductors (MOS) were found to be the most preferable solution for future applications due to their outstanding electrochemical, physical, and gas-sensing properties.[5] The advantages such as lengthy lifespan, ecofriendliness, easy miniaturization, recyclability, low-cost enhancement of mass production, and environmental sustainability of the product. Moreover, the range of target gas being detected by the MOS-based sensor is wider than the other gas sensor types and is in the concentration range from ppb to ppt.[6] For environmental monitoring of several important urban air pollutants, such as nitrogen oxides (NO_x), ozone (O_3), volatile organic compounds (VOCs), sulfur oxides (SO_x), and carbon oxides (CO_x), the operability of sensing materials, namely TiO_2, In_2O_3, SnO_2, and ZnO, have demonstrated high potential for gas-sensing and monitoring applications.[7,8]

One of the promising MOS-based nanomaterials for gas detectors is the ZnO nanostructure, which is abundantly available in nature.[9] Besides, ZnO is widely used in sensing applications owing to its excellent optical and electrical characteristics, such as low intrinsic carrier concentration ($<10^6$ cm^{-3}), high maximum n-type doping (10^{19} cm^{-3}), and its ability to achieve p-type doping ($<10^{-17}$ cm^{-3}).[10] Moreover, ZnO has a wurtzite-type hexagonal crystal structure and possesses a wide band gap energy of approximately 3.4 eV at room temperature, along with high physical and chemical stability.[11−17] Nonetheless, there are several limitations to the exploitation of the ZnO-based sensing material as a gas sensor, including poor selectivity and high power consumption due to the high operating temperature (>200 °C).[18] Moreover, the need for a heater alertly carries the risk of fire ignition of flammable liquids or gases in the monitoring environment.

Received: September 29, 2023
Revised: January 5, 2024
Accepted: February 2, 2024
Published: February 16, 2024

Table 1. Results of Previously Reported Work on CO_2 Gas Sensors

sen. material	fabrication method	working temperature	gas respectively/eqs	concentrations (ppm)	response/recovery times	refs
ZnO	chemical spray pyrolysis	350 °C	$65\%/\left(\frac{R_a-R_g}{R_a}\times 100\%\right)$	400	75/108 s	29
SnO_2	coprecipitation	240 °C	$1.24/\left(\frac{R_a}{R_g}\right)$	2000	350/4 s	30
SnO_2@CdO	hydrothermal method	30 °C	$4.20/\left(\frac{R_g}{R_a}\right)$	200	4/6 s	31
$La_2O_2CO_3$	precursor annealing	325 °C	$3.4^a/\left(\frac{R_g}{R_a}\right)$	1000	15/30 min	32
7% Gd-doped CeO_2	solution precipitation	250 °C	$45\%/\left(\frac{R_g-R_a}{R_a}\times 100\%\right)$	800	400/300 s	33
ZnO/SnO_2	chemical bath deposition	100 °C	$4/\left(\frac{R_g}{R_a}\right)$	15	19/65 s	34
reduced graphene oxide	hydrogen plasma	RT	$10\%/\left(\frac{R_a-R_g}{R_a}\times 100\%\right)$	500	4/4 min	35
$BaTiO_3$−CuO	RF sputtering	300 °C	$10\%/\left(\frac{R_g-R_a}{R_a}\times 100\%\right)$	200	2/3 min	36
p-CuO/n-$CuFe_2O_4$	RF sputtering	250 °C	$40\%/\left(\frac{R_g-R_a}{R_a}\times 100\%\right)$	5000	55/8 min	37
rGO-In_2O_3−NiO	hydrothermal treatment	RT	$40\%/\left(\frac{R_g-R_a}{R_a}\times 100\%\right)$	50	6/18 s	38

[a]Denotes a value not explicitly stated in the study but approximated from a graphical plot.

Notably, the variable thermal load (constantly changing heating and cooling processes) can induce rapid changes in the performance and shorten the durability of the ZnO gas sensor, followed by the disruption of the sensor material and electrical contacts between the metal and ZnO.[19] Nevertheless, through the optimization of morphology, structure, dopant type, and amount within the fabrication method of ZnO nanomaterials, these drawbacks can be minimized significantly.[20]

A large spectrum of nanostructures, such as nanofilms, nanorods, nanoflowers, and nanowires, for MOS-based sensors, can be effectively synthesized by hydrothermal, solvothermal, electrospinning, and DC or radio frequency (RF) magnetron sputtering techniques.[21,22] A highly ordered nanostructure (i.e., ZnO) is particularly advantageous, as it provides a larger surface area for gas adsorption and enables efficient molecular diffusion of the target gas. In order to achieve the desired characteristics, magnetron sputtering of the sensor material is particularly favorable. This method provides a reliable and nontoxic approach for the fabrication of ZnO nanorods in a vacuum environment with high purity, controllable surface morphology, and thickness.[23,24] The critical parameters are the vacuum level in the magnetron chamber, substrate temperature, and applied power, which can further increase (or decrease) the specific surface area of the ZnO thin film.[25] Furthermore, using the magnetron sputtering method at different conditions, namely codeposition (uses two or more targets) or single deposition (uses one target), it is possible to incorporate different doping elements into the main working sensitive material (ZnO). For instance, the addition of cobalt results in tuning of the band gap energy and electrical properties of ZnO at a low dopant content, thereby improving its gas-sensing response. The catalytic activity and oxidation of cobalt oxide in the presence of gases like acetone, benzene, ethanol, hydrogen gas (H_2), and carbon dioxide (CO_2) at low temperatures further elevates the response of cobalt-doped ZnO nanostructures.

The fabrication of CZO nanostructures by magnetron sputtering at room temperature (RT) provides a reliable environment for obtaining nanorods with a high surface area and uniform nanostructures.[26,27] Also, transition metal (TM) doping (Al, Ti, In, and Ni) into ZnO has been found to enhance the response and selectivity of the nanofilms toward specific gases, such as CO_x, H_2, and H_2S. For example, Li et al. synthesized CZO nanofilms by cosputtering and demonstrated their potential as CO_x sensors with high sensitivity at 350 °C.[28] There are only a few works on the application of CZO nanofilms for CO_2 gas sensing near RT. In addition, a literature survey of CO_2 sensors is presented in Table 1 and the Supporting Information (see Table S1).

The main focus of this work is the fabrication of novel CO_2 gas-sensitive CZO nanorods with improved morphological and electrical properties by the RF magnetron sputtering method. The morphological and structural properties of the sputtered thin films were characterized using scanning electron microscopy (SEM), X-ray diffraction analysis (XRD), atomic force microscopy (AFM), photoluminescence spectroscopy (PL), Fourier-transform infrared spectroscopy (FTIR), and UV−vis spectroscopy. The CZO-based gas sensors were prepared by direct deposition of thin films on integrated gold microelectrodes on glass substrates. The gas-sensing performance of the obtained device was studied at various CO_2 gas concentrations (1−1500 ppm) at RT. The gas response properties showed that the fabricated sensor exhibited a high gas response and more selective and relatively stable features for CO_2 gas at RT.

EXPERIMENTAL SECTION

Target Preparation for RF Magnetron Sputtering. The ammonium cobalt(II) sulfate hexahydrate salt was treated thermally (300 °C for 6 h) to obtain cobalt oxide (Co_3O_4) powder. Zinc oxide (ZnO) and Co_3O_4 powders were mixed in an ethanol medium and homogenized in a grinding chamber for 12 h at 400 rpm for better distribution of the precursor materials. The wet material was then dried in an oven at 60 °C for 48 h and granulated through a sieve of 0.9 mm. The granules were further treated thermally at 400 °C for 4 h with subsequent sieving at similar conditions. After that, to achieve complete crystallization, the material was sintered at 800 °C for 4 h.

https://doi.org/10.1021/acssensors.3c02059
ACS Sens. 2024, 9, 1227−1238

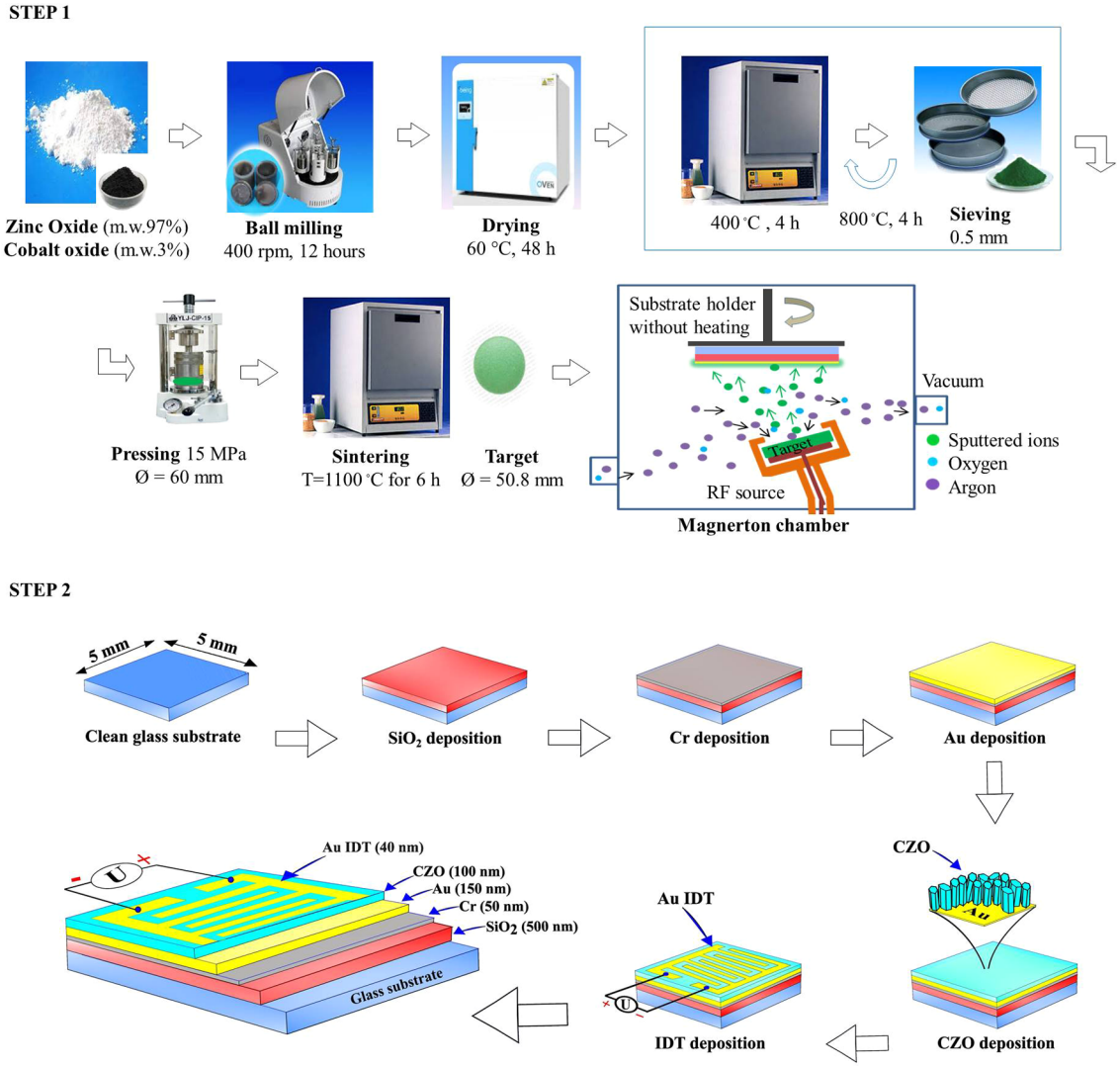

Figure 1. Schematic illustration of the preparation of the CZO target (Step 1) and the deposition of CZO thin films by RF magnetron sputtering (Step 2).

Table 2. Magnetron Sputtering Deposition Parameters of ZnO and CZO Thin Films

sample name	target name	RF power (W)	tooling factor (%)	deposition rate (nm/s)	average thickness (nm)
ZnO	pure ZnO	45	95	0.032 ± 0.011	85.64 ± 0.12
CZO-45W	Co-doped ZnO	45	112.5	0.045 ± 0.004	97.55 ± 0.11
CZO-60W	Co-doped ZnO	60	110.3	0.057 ± 0.003	110.07 ± 0.14
CZO-75W	Co-doped ZnO	75	109.8	0.118 ± 0.005	111.67 ± 0.09

The powders were pressed into a pellet disc with a diameter of Ø = 60 mm and a height of 3 mm by applying a pressure of 15 MPa. Additional sintering at 1100 °C for 6 h at a heating rate of 3 °C per minute allowed the pressed discs to be transformed into solid ceramic bodies. Finally, a solid CZO target was obtained for deposition by RF magnetron sputtering. Schematic illustration of the preparation of the CZO target and the deposition of CZO thin films by RF magnetron sputtering are shown in Figure 1.

The CZO sensor devices were manufactured on silicon dioxide (SiO_2)-coated glass with a Cr layer and gold (Au) electrode. A self-made target for magnetron sputtering was prepared, as shown in Figure 1 (Step 1). The Cr layer acts as a diffusion barrier where the top electrode layer is prevented from diffusing into the substrate, allowing a low-resistance contact to be made with the material. The Cr layer also helps improve the adhesion between the substrate and the top electrode layer, which is important for the long-term stability and performance of the device. The IDT contacts were manufactured by Au sputtering with a thickness of 40 nm over the CZO layer using an aluminum mask, as shown in Figure 1 (Step 2).

Preparation of CZO Thin Films. CZO thin films were deposited on glass substrates without additional heating using the RF magnetron sputtering technique.[39] The substrates were ultrasonically cleaned in ethanol and acetone, rinsed in deionized water, and air-dried before deposition. For the sputtering deposition, the working chamber was vacuumed to reach a base pressure of 3×10^{-7} mbar. The substrates were fixed at a distance of 6 cm from the CZO target surface. The CZO thin films were deposited with a mixture of reactive gases (pure argon (Ar) and oxygen (O_2), 5:1) inside the chamber. The gas purities were 99.9996% for Ar and 99.9995% for O_2. Presputtering was carried out for 40 min to clean and equilibrate the target surface prior to deposition. The same conditions were used for sputtering and sputtering, except for the deposition rate. During the deposition of

https://doi.org/10.1021/acssensors.3c02059
ACS Sens. 2024, 9, 1227−1238

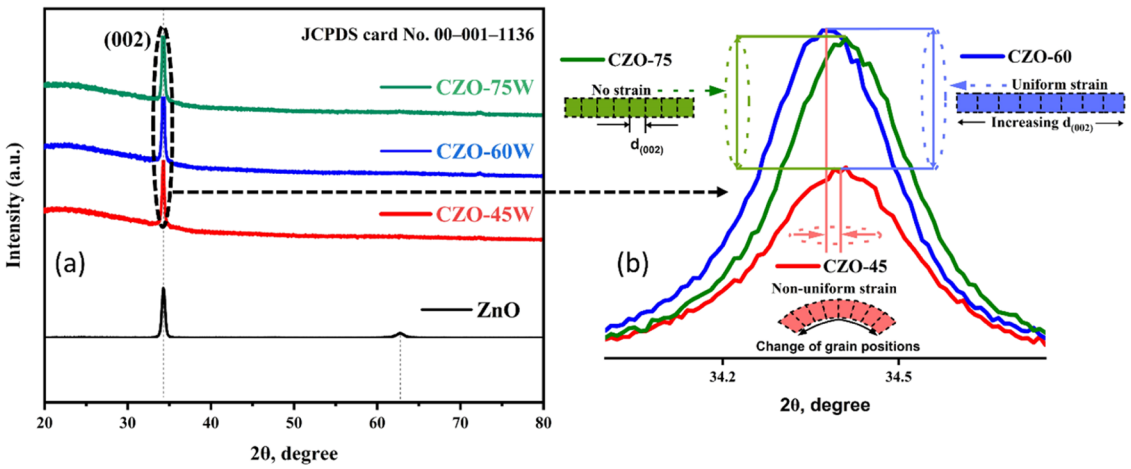

Figure 2. XRD spectra of (a) ZnO and CZO thin films and (b) the effect of strain on the (002) peak.

Table 3. Structural Parameters of ZnO and CZO Thin Films Obtained from XRD

			lattice parameter [Å]					
sample name	D [Å]	FHWM [Å]	$a = b$	c	V [Å^3]	$d_{(002)}$ (Å)	δ (Å)$^{-2} \times 10^{-6}$	ε (10^{-3})
ZnO	17.51	0.496	3.007	5.210	40.82	2.605	3.26	6.9
CZO-45W	27.74	0.313	3.008	5.210	40.83	2.605	1.30	4.4
CZO-60W	32.04	0.271	3.010	5.213	40.90	2.607	0.97	3.8
CZO-75W	32.25	0.269	3.007	5.208	40.78	2.604	0.96	3.8

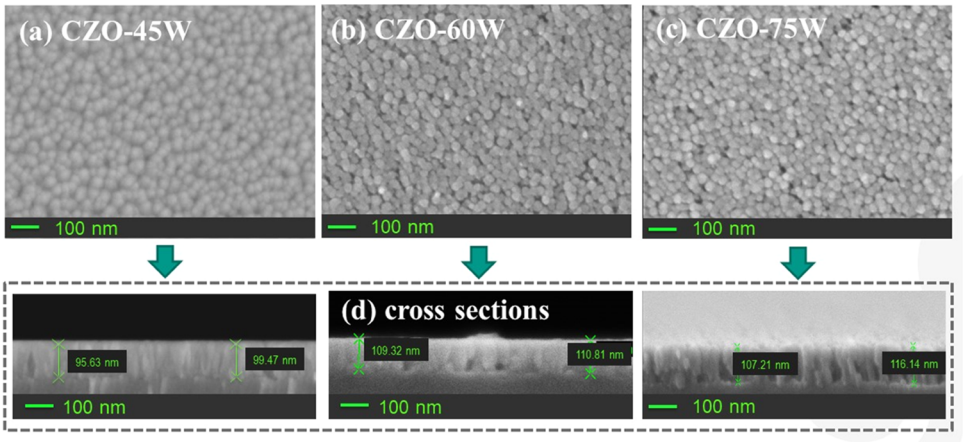

Figure 3. SEM images of the CZO thin films deposited at different RF powers: (a) 45, (b) 60, and (c) 75 W. (d) Cross sections of CZO thin films.

CZO films, the total pressure was maintained at 5 mTorr, with a gas flow of 20 sccm. The input powers at the target were 45, 60, and 75 W. The deposition rates and durations used for the production of CZO thin films are shown in Table 1. The deposition rates varied from 0.013 to 0.068 nm/s with RF power. Full details of the preparation procedure for the CZO gas sensor device with Au IDT electrodes are provided in Table 2.

Characterization of CZO Films. The phase composition and crystal structure of all thin films were carefully examined using XRD (SmartLab Rigaku; Cu Kα_1 was used as a radiation source, λ = 0.15406 nm, tube voltage, and tube current were 30 kV and 25 mA, respectively, scanning speed was 0.02°/s, scanning range was 20–80°). The surface morphology of the CZO thin films was studied via SEM (ZEISS Crossbeam 540). The chemical components were inspected by X-ray photoelectron spectroscopy (XPS) (NEXSA, Thermo Scientific) and energy dispersive spectroscopy (EDS) (JSM-IT200). AFM (SmartSPM 1000) analysis was performed to investigate the roughness distribution of nanoparticles. The thicknesses of the CZO nanofilms were quantified by a stylus profilometer (Dektak XT Stylus Profiler). The Hall effect analysis of the thin films was performed via an HMS-5500 equipment system with a constant magnetic field of 0.55 T. Optical properties of the CZO thin films were determined by UV–vis spectrophotometer (Evolution 300 UV–vis) within the wavelength range of 200–1000 nm. Measurements of the gas response of the sensors were provided by the gas measurement unit "GMS-311". The gas measurements of the gas sensors were done at room temperature (RT ~ 27 °C) for different CO_2 gas concentrations (1–1500 ppm). The best working gas concentration for the fabricated gas sensors was then specified. Some gas-sensing measurement parameters, such as gas response, selectivity, and stability, were investigated for a full understanding of the quality of the produced gas sensors. The gas response of the CZO sensors was estimated using the relation $\mathbf{S} = \mathbf{R}_{air}/\mathbf{R}_{gas}$. The gas-sensing measurements of the fabricated sensors for CO_2 and different gases were carried out by using a computer-controlled device. The setup consists of a current–voltage source measurement unit (Keithley-2450), a temperature controller (SRS Stanford Research Systems – CTC100), gas flow controllers (MFC-1 and MFC-2), a humidity sensor, a test chamber, a digital interface unit, gas cylinders (dry air and target gas CO_2), and a PC. A clear, detailed schematic of the

https://doi.org/10.1021/acssensors.3c02059
ACS Sens. 2024, 9, 1227–1238

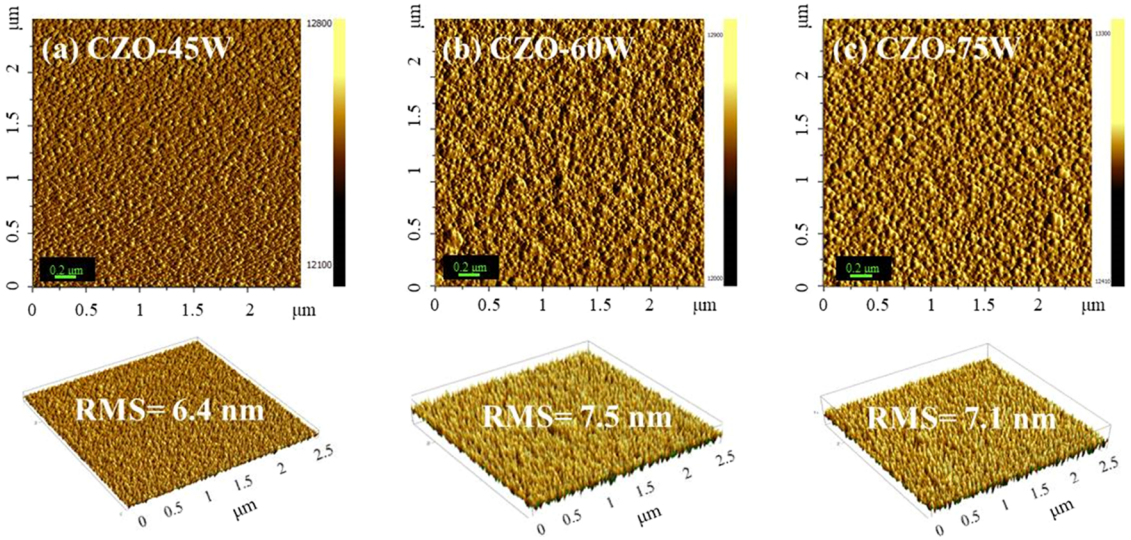

Figure 4. AFM images (2D and 3D) of the CZO thin films grown by RF sputtering at various RF powers: (a) 45, (b) 60, and (c) 75 W.

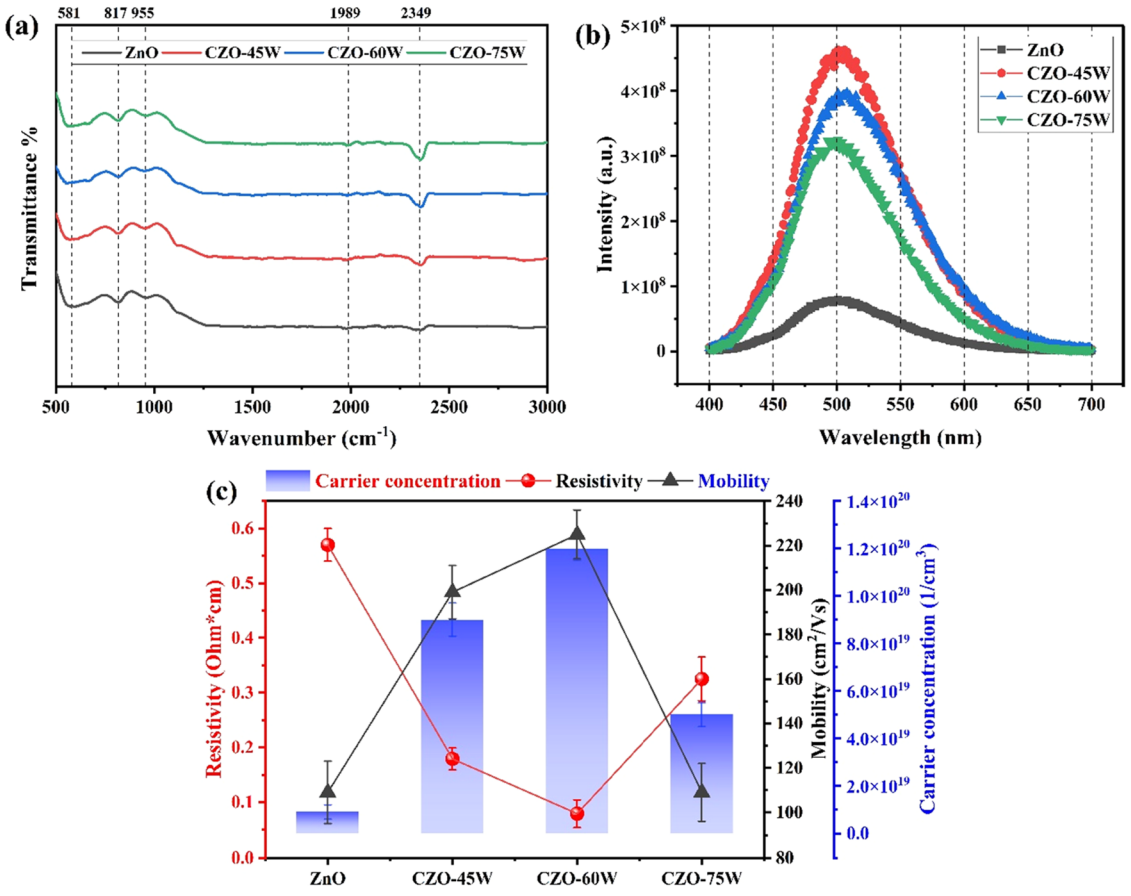

Figure 5. (a) FTIR spectra, (b) PL, and (c) Hall measurement results of ZnO and CZO thin films.

sensing setup and gas measurements is provided in the Supporting Information (see Figure S1).

RESULTS AND DISCUSSION

Microstructural and Morphological Characterization of the Produced Thin Films. The influence of increasing RF sputtering power on the structures of the ZnO and CZO (CZO-45W, CZO-60W, CZO-75W) thin films was determined by XRD. As evident in Figure 2a, CZO thin films reveal a strong preferential orientation toward the (002) plane of polycrystalline hexagonal ZnO with minor changes in the characteristic parameters reported in Table 3. The peak intensity of the CZO thin films increased, along with a shift in the peak positions from 34.39 to 34.37°, reaching 34.41° at 45, 60, and 75 W, respectively. All the peak angles are in good agreement with the *c*-axis-oriented ZnO (002) peak from JCPDS card No. 00−001−1136 at 34.4°. CZO-60 W displayed an expansion in volume and lattice parameters as well as a

https://doi.org/10.1021/acssensors.3c02059
ACS Sens. 2024, 9, 1227−1238

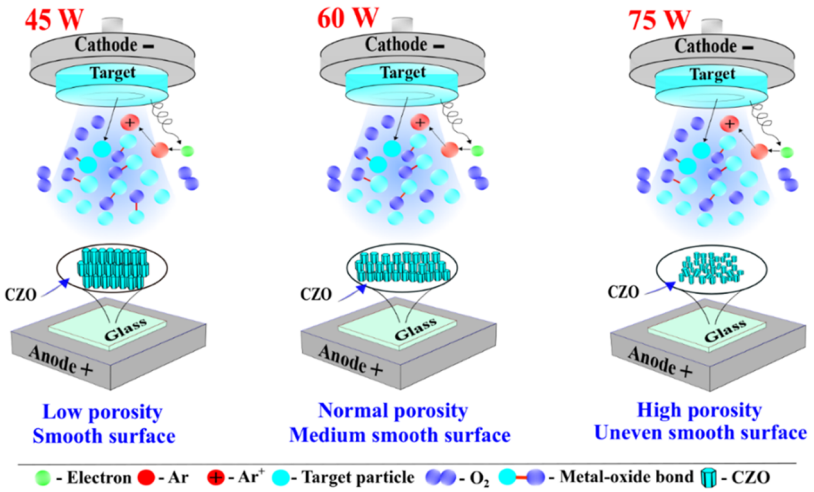

Figure 6. Illustration of the effect of the deposition rate on the formation of CZO thin films.

uniform strain throughout the crystal lattice, as shown in Figure 2b.[40] The trends of shrinking full width at half-maximum (fwhm) and the growing crystallite size in Table 3 are similar to the results reported by Gonçalves et al.[25] at RF powers of 50 and 75 W.

The changes in the surface morphology and topography of the CZO thin films due to the increase in the power of magnetron sputtering were analyzed using SEM and AFM. From Figure 3a–c, it can be seen that the shape of the particles sputtered at 45W is close to a sloped cylinder, while at higher powers of sputtering, 60 and 75 W, the thin films are composed of more vertically inclined rod-like particles with a defined hexagonal shape observed from the top view. Although the films were sputtered uniformly, a visible increase in the particle densities of CZO-60W and CZO-75W thin films was observed. Figure 3d demonstrates the changes in particle heights as they increase due to the higher energy of sputtering in accordance with Table 2.

The AFM micrographs taken for 2.5 μm × 2.5 μm area and shown in Figure 4a–c allow access to the difference qualitatively and quantitatively regarding the surface topography of CZO thin films that appear to be nucleated as individual, conical islands. It is widely known that optimal surface roughness should be achieved to attain proper gas sensing, as an increase in this parameter generally leads to an increase in the number of adsorption sites for oxygen molecules.[41,42] The root-mean-square (RMS) value of 7.5 nm for CZO-60 W was found to be higher than that of CZO-45W and CZO-75W thin films, 6.4 and 7.1 nm, respectively. Quite possibly, the deposition power of 60 W results in the highest total surface area of the prepared material due to the intermediate grain size and highest RMS value.[43] These results suggest that the morphology and topography of the CZO thin films were significantly affected by the power applied to the RF source as the main deposition condition.

Optical and Electrical Properties of CZO Thin Films. The FTIR spectra of the fabricated ZnO and CZO films, such as CZO-45W, CZO-60W, and CZO-75W sensors, are shown in Figure 5a. The FTIR results were performed for the CZO thin films using the KBr pellet method in the wavenumber range of 500–3000 cm^{-1}. All of the CZO thin films exhibited absorption bands at 2349, 1989, 955, 817, and 581 cm^{-1}. The absorption bands at 581 and 817 cm^{-1} are attributed to the Zn–O stretching in the ZnO lattice.[44] The absorption peaks observed at 2349 and 1989 cm^{-1} are related to the existence of CO_2 molecules in air.[45] The medium to weak band at 955 cm^{-1} is assigned to the metal–oxygen vibration frequency due to the changes in the microstructural features (see the XRD results and Table 3) by the increase of the amount of cobalt (CZO-45W, CZO-60W, and CZO-75W) in the Zn–O lattice. In addition, the band gap energies of the CZO thin films were calculated by UV–vis spectroscopy and are provided in the Supporting Information (see Figure S2). A detailed investigation of the existence of the structural defects in the CZO thin film was carried out by PL. Figure 5b shows the PL spectra of the pure ZnO and CZO samples at room temperature in the 400–700 nm wavelength range. In the case of ZnO, the near band emission of crystal defects is typically observed in the UV region (<400 nm) with a sharp peak, while the deep level emission (DLE) is usually observed in the visible light area (>400 nm) with a broad peak.[46] In accordance with many theoretical and experimental PL results, it can be assumed that the visible emissions are related to the substitution of oxygen atom to zinc atom position represented by a variety of intrinsic abnormalities, such as oxygen vacancies (V_O), interstitial oxygen (O_i), antisite oxygen (O_a), and zinc vacancies (V_{Zn}), among others.[47] In the visible light region, the ZnO and CZO thin films exhibit similar line shapes with one PL peak at 500 nm, as seen in Figure 5b. These results are in line with the literature,[48] which is explained by the recombination of electrons and twice-ionized oxygen vacancies (V_O) with photogenerated holes in the ZnO lattice.[49] Broad blue emission at 484 nm bands is typically attributed to the radiative recombination of oxygen vacancies and electrons.[50] It has been found that the intensity of the DLE of CZO samples decreases noticeably with increasing RF sputtering power. In the case of CZO-75W, the PL intensity is observed to be slightly lower than those of the CZO-45W and CZO-60W samples, which may be ascribed to the increase in V_O, O_i, or Zn_i defects.

Hall effect studies were carried out to obtain the Hall parameters, such as resistivity (ρ), Hall mobility (μ), and carrier concentration (n) by HMS-5500. According to the Hall measurement results, the carrier concentration of the ZnO increased when Co atoms were introduced, and the maximum value corresponded to CZO-60W ($n = 1.3 \times 10^{20}$ $1/cm^3$). This value is smaller for the sample CZO-75W, which was

https://doi.org/10.1021/acssensors.3c02059
ACS Sens. 2024, 9, 1227–1238

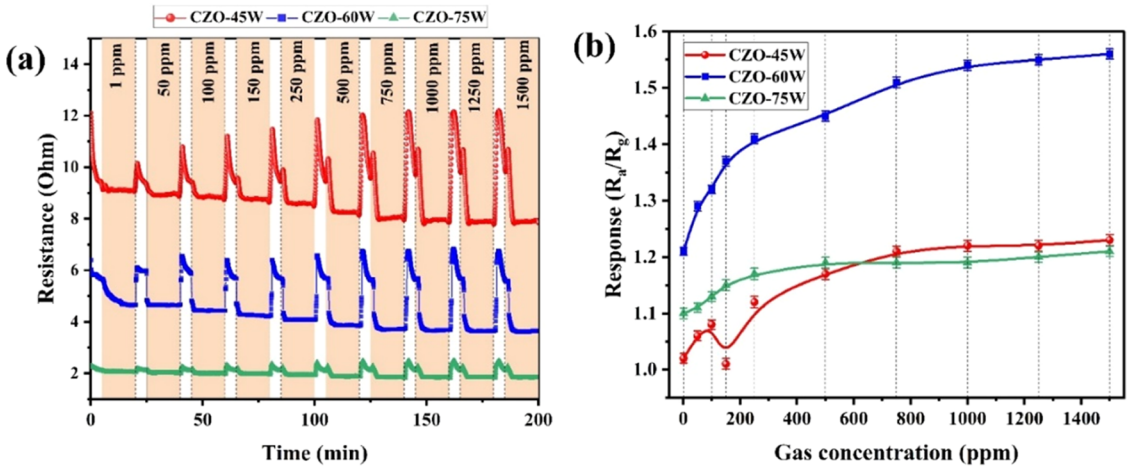

Figure 7. (a) Resistance changes and (b) responses of CZO-45W, CZO-60W, and CZO-75W sensors to CO_2 at gas concentrations of 1−1500 ppm.

sputtered under the same conditions, except for the applied magnetron power of 75 W. In a comparable way, as evidenced by the same graph, the electrical resistivity of CZO-60W has shown the lowest value of around 0.08 Ω·cm and increases for CZO-75W. As is known, the resistance and conductivity properties of CZO thin films obtained using magnetron sputtering strongly depend on the parameters of the magnetron sputtering system (i.e., depends on power and deposition rate). It is very important to obtain a homogeneous film by the sequential application of layers. In this work, thin films of ZnO and CZO were obtained by using magnetron sputtering by varying the device power to 45, 60, and 75 W, respectively. However, at a 75 W power, electrical properties such as carrier concentration, resistivity, and mobility deteriorate sharply, as shown in Figure 5c. This may be due to an increase in the deposition rate. As shown in Table 2, the deposition rate at 75 W increases sharply (almost 2 times) compared with that at 45 and 60 W. Rapid deposition can limit the time required for grain growth, which in turn will affect the microstructure, crystallinity and uniformity of the dopant distribution of ZnO/CZO. Moreover, the surface smoothness and porosity of the thin films are important parameters that are maintained by the deposition rate. Figure 6 clearly shows examples of the formation of CZO thin films at various deposition powers, such as 45, 60, and 75 W. The slow deposition rate (45W) promotes the formation of compact grains with smooth surfaces and reduces defects in the structure. Under such conditions, the particles have enough time to organize into compact structures, ensuring a high degree of adhesion and surface uniformity. As the deposition rate increases (60 and 75 W), a reduction in grain size is observed as the nuclei do not have time to fully form. This effect is accompanied by an increase in the porosity and various types of defects in the film. In the context of gas sensors, the formation of defects can lead to an increase in the number of vacant sites for oxygen, which in turn increases the gas response of the sensing material (CZO thin films). Thus, setting up the experiment makes it possible to determine the optimal limit of proper control for producing CZO thin films by RF magnetron sputtering.

In addition, the inhibitory effect of such doping on the production of O_2-derived defects at the ZnO grain boundary surfaces is the possible reason for the decrease of resistivity that occurred after the introduction of Co dopant into the ZnO matrix.[51] For CZO-75W, the observed decrease in the *n* carriers can be accounted for by the Zn vacancies (V_{Zn}), which can induce the acceptor level, while oxygen vacancies behave as deep donors and Zn as shallow donors.[52]

Gas-Sensing Properties of the CZO Sensors. Figure 7 depicts the resistance-time change reaction of the CZO sensors when exposed to CO_2 gas ranging from 1 to 1500 ppm at room temperature under dry air. As shown in Figure 7a, the gas sensor exhibits a nonlinear change in the concentration versus gas response. This pattern is consistent with the observations reported in various studies.[53−55] These studies emphasized nonlinear trends extending beyond certain concentrations according to the $S \sim C^n$ dependence. In this study, the gas response exhibits a consistent linear relationship within the 1−300 ppm range. However, as the concentration increases, a discernible shift toward nonlinear behavior becomes increasingly evident. Furthermore, the enhanced performance of the CZO-60W sensor is unmistakably apparent when compared to its CZO-45W and CZO-75W counterparts. Specifically, CZO-60W demonstrates superior gas response at room temperature in the presence of dry air. It demonstrates a heightened response at various concentration levels: 1, 50, 100, 150, 250, 500, 750, 1000, 1250, and 1500 ppm, with corresponding response values of 1.2, 1.29, 1.32, 1.37, 1.41, 1.45, 1.51, 1.54, 1.55, and 1.56, respectively. The variance observed in the gas responses of these sensors can be attributed to the distinct morphology of the sensing surface pertinent to each sensor type. The introduction of Co doping leads to an increased occurrence of point defects and oxygen vacancies within the CZO sensors.[56] This augmentation contributes to the enhanced gas response in contrast to undoped ZnO sensors. The relationship between the CO_2 gas concentration and the corresponding sensor response was deduced, as depicted in Figure 7b.

Additionally, the gas-sensing capabilities of the developed gas-sensing materials (CZO thin films) were tested at RT under various relative humidity (RH) conditions. The impact of RH on gas sensitivity was examined at 25, 50, and 75% RH, respectively, utilizing a humidity controller with an accuracy of ±0.1% RH, which was integrated into the gas measurement system. Humidity tests revealed that the resistance of the sensors decreases with humidity in dry air from ∼3.8 to ∼3.3 Ω at 50% RH for CZO-60W. This phenomenon was also

https://doi.org/10.1021/acssensors.3c02059
ACS Sens. 2024, 9, 1227−1238

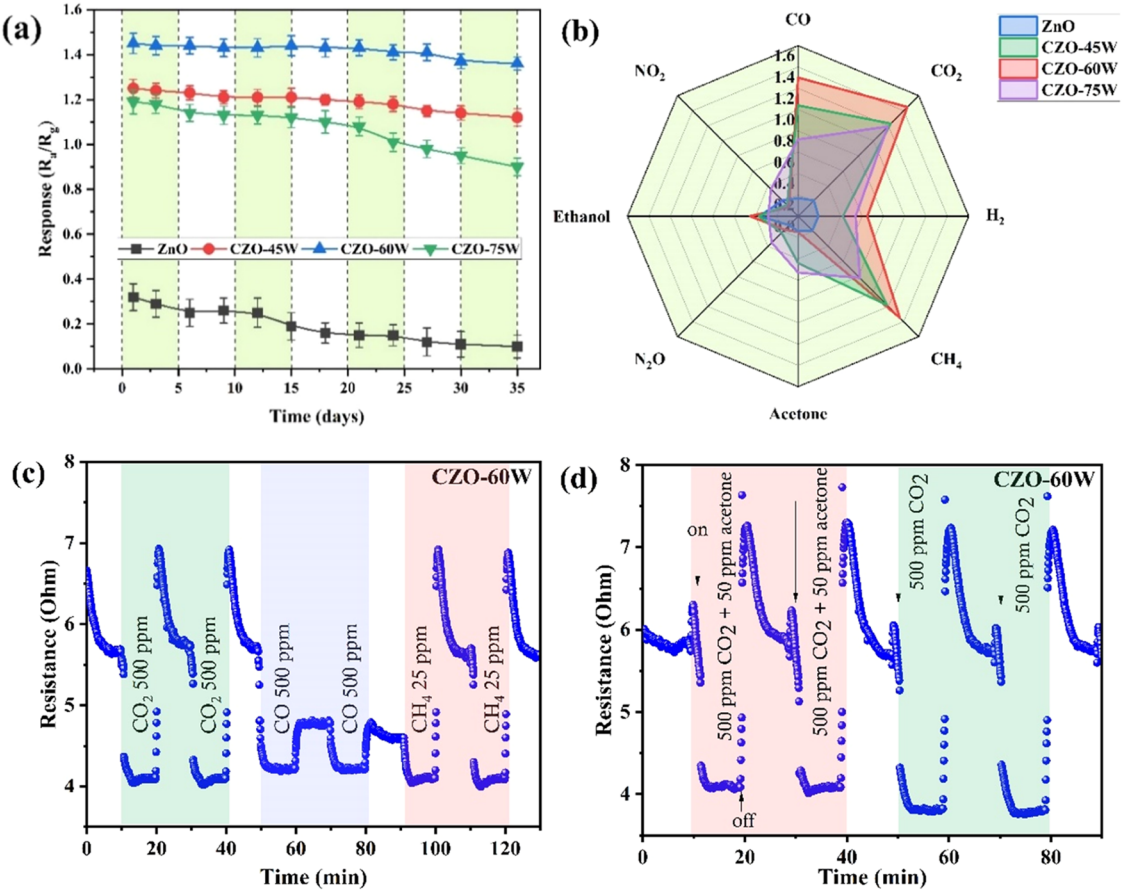

Figure 8. (a) Stability and (b) selectivity results of the fabricated CZO sensors for 500 ppm of different target gases at RT; cross-selectivity measurements of the CZO-60W sensor (c) with CO and CH_4 and (d) a mixture of CO_2 and acetone.

detected for the other CZO-45W and CZO-75W sensors (see Figure S3, Supporting Information). The decrease in the gas response is a result of increased electron concentration within the sensing material, which is attributed to the absorption of water molecules on the surface of the sensing material.

We evaluated the stability performance of the CZO-based sensors (CZO-45W, CZO-60W, and CZO-75W) by exposing them to 500 ppm CO_2 gas for one month, as shown in Figure 8a. Among these devices, the CZO-60W gas sensor exhibited a remarkably stable response (R_a/R_g = 1.45), which subsequently decreased to an acceptable value (R_a/R_g = 1.39) for the gas response. The sensor's stability decreased due to the adsorption of moisture from air. Interestingly, the gas response of the CZO-60W sensor increased at the optimal ratio (~1.8) of Co/Zn (see Table S2, ICP results, Supporting Information). Indeed, when CO_2 gas molecules are present in the gas chamber, they can be adsorbed on the surface of the gas sensor and occupy the adsorption sites. Therefore, the number of adsorption sites and surface defects increased (see the PL results), leading to higher adsorption reactions of CO_2 gas molecules and resulting in a high gas response of the CZO gas sensors. Finally, we examined the selectivity and cross-sensitivity of the CZO gas sensors by exposing them to 500 ppm CO, CO_2, CH_4, N_2O, NO_2, H_2, acetone, and ethanol. Figure 8b presents the gas selectivity pattern of the CZO gas sensor in response to the aforementioned gases. The corresponding CO_2 gas responses were evaluated for CZO-45W, CZO-60W, and CZO-75W, respectively.

Cross-sensitivity studies are pivotal in gas sensor development to ensure improved specificity and accuracy. By investigating how sensors respond to various gases, these studies contribute to enhanced selectivity, reliability, and overall performance, which are crucial for gas sensor applications.[57] In our work, the developed CZO-based sensing materials have demonstrated high selectivity properties upon consecutive exposure (CO_2, CO, and CH_4) and when exposed to a mixture of CO_2 and acetone (see Figure 8c,d). It was observed that certain gases influenced the resistance background level, potentially indicating low desorption. However, this effect is reversible after exposure to other gas types, such as methane, in our tests. The sensing material was stable in the presence of a mixture of CO_2 and acetone (500 + 50 ppm), with the response value changing by 5% (R_a/R_g shifting from 1.50 to 1.43). Notably, the background value remains consistent before and after the exposure to the gas mixture. The high selectivity can potentially be explained through ab initio calculations of the adsorption energy. Thus, the CZO-60W sensor showed excellent selectivity for CO, CO_2, and CH_4 gases.

Gas-Sensing Mechanism. The gas-sensing mechanism in MOS-based sensing materials is often explained by the surface conductivity theory.[58] According to this theory, the interaction between the metal oxide surface and gas molecules induces changes in material conductivity, serving as a sensitive indicator of gas presence and concentration. This phenomenon is rooted in the adsorption and desorption processes with factors such as chemisorption, physisorption, defects, grain

https://doi.org/10.1021/acssensors.3c02059
ACS Sens. 2024, 9, 1227−1238

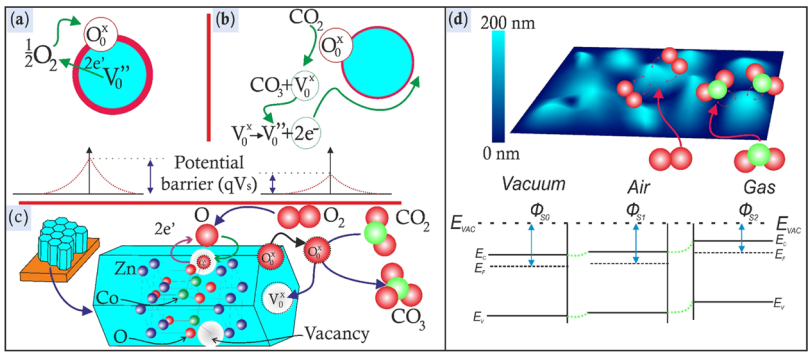

Figure 9. Schematic illustration of the CZO gas sensor with CO_2 target gas: reaction mechanism and energy level of the CZO gas sensor (a) before and (b) after exposure to CO_2 gas; (c) schematic diagram of the corresponding energy band structure of CZO; and (d) physisorption-based gas-sensing mechanism with a shift in the work function under exposure to different gases.

Table 4. Summary of the Recently Reported CZO Gas Sensors

fabrication method	optimal doping content	optimal temperature	eqs/approximate sensitivity	gas concentration (ppm)	response/recovery times (s)	gas type	refs
chemical bath deposition	5 mM	300 °C	$\left(\frac{R_a - R_g}{R_g} \times 100\right)$–90.71%	100	14/28	ethanol	63
hydrothermal method	3.1 atom %	210 °C	$\left(\frac{R_g}{R_a}\right)$–88	500	90/80	NO_x	64
electrospinning	0.5 wt %	360 °C	$\left(\frac{R_a}{R_g}\right)$–16	100	6/4	acetone	65
hydrothermal method	15 wt %	100 °C	$\left(\frac{R_a - R_g}{R_a} \times 100\right)$–86.1%	50	19.4/15.5	trimethylamine	66
coprecipitation method	25 wt %	100 °C	$\left(\frac{R_a - R_g}{R_a} \times 100\right)$–70.6%	100	55/35	p-xylene	62
hydrothermal/electrochemical method	1.85 atom %	350 °C	$\left(\frac{R_a}{R_g}\right)$–10.9	50	60/180	CO	28
chemical spray pyrolysis	5 wt %	RT	$\left(\frac{R_a}{R_g}\right)$–800	50	250/40	acetaldehyde	61
magnetron sputtering	2.5 atom %	150 °C	$\left(\frac{R_a - R_g}{R_a} \times 100\right)$–69%		120/300	hydrogen	67
magnetron sputtering	1.81 atom % (60 W)	RT	$\left(\frac{R_a}{R_g}\right)$–1.45	500	72/35	CO_2	this work

boundaries, and surface morphology, which contribute to the overall gas-sensing performance of CZO. Understanding these complex interactions is crucial for optimizing the design and efficacy of CZO-based gas sensors. The resistivity of the sensors depends on the concentration of oxygen vacancies, which occur by the doping of Co^{3+} into the ZnO lattice, as shown in Figure 9a–c. Oxygen atoms react with the positive oxygen vacancies to form oxygen ions at their lattice sites.

$$V_O'' + 2e\,(CB) + \frac{1}{2}O_2\,(gas) \leftrightarrow O_O^x \quad (1)$$

This reaction reduces the conductivity of the sensor, as ZnO loses electrons in the presence of an oxygen environment.

The CO_2 gas reacts with O_O^x to form metastable carbon tetroxide (CO_3).[59]

$$CO_2\,(ads) + O_O^x \leftrightarrow CO_3\,(gas) + V_O^x(2) \quad (2)$$

CO_3 has a short lifetime; thus, it further dissociates into CO_2 and O_2.

The neutral oxygen vacancies ionize to give electrons back to the conduction band:

$$V_O^x \leftrightarrow V_O^{**} + 2e^- \quad (3)$$

Thus, the adsorption of CO_2 gas onto ZnO increases the free carrier concentration and the conductivity increases upon exposure to CO_2 gas. An additional physisorption mechanism is illustrated in Figure 9d. Physisorption does not result in electronic structures or electron transitions, as no chemical bonds occur. However, there is a uniform upward shift in the work function of the sensing layer, ranging from Φ_{S1} to Φ_{S2} by a specific value.[60] It is noteworthy that within this investigation, two observed phenomena substantiate the binary nature of the sensory properties: physisorption and chemisorption, as confirmed by experimental data (see Figure S4, Supporting Information).

Notably, with a medium vacuum level (5 mTorr) and optimal power of the magnetron source (60 W), we achieved a huge enhancement of the gas response for the CZO-based sensor compared to ZnO (as a control sample) at a CO_2 concentration of 500 ppm at RT. This can be explained by the variation in the morphological and electrical phenomena on the CZO sensor's surface. Moreover, the addition of Co

https://doi.org/10.1021/acssensors.3c02059
ACS Sens. 2024, 9, 1227–1238

dopant into the ZnO nanostructure contributes to the formation of oxygen vacancies (see Figure S5, Table S3—XPS results, and Figure S6—SEM/EDX results in the Supporting Information), which can increase the carrier density and accelerate the electron transfer during the CO_2 gas reaction. This work presents a reliable CO_2-sensing material that has a high sensing response at RT and expands on the effect of sputtering power through a variety of characterization methods. Similar to this work, Mani et al. reported a CZO nanostructure that is very sensitive at room temperature, albeit for acetaldehyde gas.[61] Increasing interest in the doping of ZnO by the cobalt element can be explained due to its large solubility in the ZnO matrix and an ionic radius (0.58 Å) similar to that of Zn (0.60 Å), which makes it a promising candidate for doping among TMs.[62] A list of recently reported CZO-based gas sensors is listed in Table 4. This study's CZO gas sensor study exhibits several favorable characteristics when compared to similar CZO sensors, including a relatively low operating temperature (RT), minimal doping content (1.81 atom %), and a quick response time (72 s).

CONCLUSIONS

In conclusion, CZO thin films (CZO-45W, CZO-60W, and CZO-75W) were successfully fabricated on glass substrates by the RF magnetron technique using a cost-effective and self-made target. The XRD results revealed that all thin films were polycrystalline with a hexagonal wurtzite crystal structure (ZnO) with a preferential orientation toward the (002) plane. All of the peak angles are in good agreement with the *c*-axis-oriented ZnO (002) peak from JCPDS card No. 00−001−1136 at 34.4°. According to the AFM outputs, an RMS value of 7.5 nm for CZO-60W was found to be higher than that of the CZO-45W and CZO-75W thin films, 6.4 and 7.1 nm, respectively. XPS measurements demonstrated the presence of oxygen vacancies (V_O) in the CZO thin films, where CZO-60W had a higher intensity than the CZO-45W and CZO-75W samples. The gas-sensing properties of sensors made from CZO nanostructures were examined across a range of CO_2 concentrations from 1 to 1500 ppm. The gas responses and response/ recovery times of the sensors were assessed at different CO_2 levels. The CZO-45W sensor exhibited a low response $\left(\frac{R_a}{R_g} = 0.36\right)$ with a response time of 77 s. Meanwhile, the CZO-60W sensor displayed an even higher response $\left(\frac{R_a}{R_g} = 1.45\right)$ and a faster response time of 72 s. The superior performance of the CZO-60W sensor can be attributed to its greater capacity for CO_2 molecule adsorption within its structure, owing to its higher RMS and the presence of defects (V_O). Additionally, both sensors exhibited a linear increase (up to 300 ppm) in gas response with an increasing CO_2 gas concentration. These findings underscore the potential of CZO-based sensors for CO_2 gas detection applications and offer a promising path for the investigation and development of low-cost and energy-efficient advanced CO_2 sensors.

ASSOCIATED CONTENT

Supporting Information

The Supporting Information is available free of charge at https://pubs.acs.org/doi/10.1021/acssensors.3c02059.

CO_2 sensing reports with surface morphology and selectivity comparison along with other essential parameters; schematic illustration of the gas-sensing measurement system; UV−vis absorption spectra of CZO-45W, CZO-60 W, and CZO-75 W thin films; the resistance changes of the CZO sensors at different humidity conditions; the resistance changes of the CZO-60W sensor in air and Ar environments; ICP results of the CZO samples; XPS O 1s scan of the CZO thin films; oxygen states of the CZO samples by XPS, and SEM/EDX images of the CZO thin films (PDF)

AUTHOR INFORMATION

Corresponding Authors

Baktiyar Soltabayev − *National Laboratory Astana, Nazarbayev University, Astana 010000, Kazakhstan;* orcid.org/0000-0002-5320-2576; Email: baktiyar.soltabayev@nu.edu.kz

Almagul Mentbayeva − *Department of Chemical and Materials Engineering, School of Engineering and Digital Sciences, Nazarbayev University, Astana 010000, Kazakhstan;* orcid.org/0000-0001-9132-1173; Email: almagul.mentabyeva@nu.edu.kz

Authors

Yessimzhan Raiymbekov − *Department of Chemical and Materials Engineering, School of Engineering and Digital Sciences, Nazarbayev University, Astana 010000, Kazakhstan*

Aidarbek Nuftolla − *Department of Chemical and Materials Engineering, School of Engineering and Digital Sciences, Nazarbayev University, Astana 010000, Kazakhstan*

Amanzhol Turlybekuly − *National Laboratory Astana, Nazarbayev University, Astana 010000, Kazakhstan*

Gani Yergaliuly − *National Laboratory Astana, Nazarbayev University, Astana 010000, Kazakhstan; Faculty of Physics and Technology, L.N. Gumilyov Eurasian National University, Astana 010000, Kazakhstan*

Complete contact information is available at: https://pubs.acs.org/10.1021/acssensors.3c02059

Author Contributions

The manuscript was written and edited with contributions from all authors. Y.R. and A.N. conducted the fabrication of CZO thin films. G.Y. and A.T. performed and analyzed all gas-sensing experiments. B.S. and A.M. were involved in planning, discussions, editing, and manuscript supervision. All authors have approved the final version of the manuscript.

Notes

The authors declare no competing financial interest.

ACKNOWLEDGMENTS

This research was funded by the Science Committee of the Ministry of Science and Higher Education of the Republic of Kazakhstan (Grant No. AP13067814) and Nazarbayev University under the Collaborative Research Program (Grant No. 021220CRP0122).

REFERENCES

(1) Wang, Z.; Bu, M.; Hu, N.; Zhao, L. An Overview on Room-Temperature Chemiresistor Gas Sensors Based on 2D Materials:

Research Status and Challenge. *Composites, Part B* **2023**, *248*, No. 110378.
(2) Uma, S.; Shobana, M. K. Metal Oxide Semiconductor Gas Sensors in Clinical Diagnosis and Environmental Monitoring. *Sens. Actuators, A* **2023**, *349*, No. 114044.
(3) Yamazoe, N. Toward Innovations of Gas Sensor Technology. *Sens. Actuators, B* **2005**, *108*, 2−14.
(4) Zhao, Y.; Liu, Y.; Han, B.; Wang, M.; Wang, Q.; Zhang, Y. Fiber Optic Volatile Organic Compound Gas Sensors: A Review. *Coord. Chem. Rev.* **2023**, *493*, No. 215297.
(5) Krishna, K. G.; Parne, S.; Pothukanuri, N.; Kathirvelu, V.; Gandi, S.; Joshi, D. Nanostructured Metal Oxide Semiconductor-Based Gas Sensors: A Comprehensive Review. *Sens. Actuators, A* **2022**, *341*, No. 113578.
(6) Tang, H.; Gao, C.; Yang, H.; Sacco, L.; Sokolovskij, R. Electronic Supplementary Information Room Temperature Ppt-Level NO 2 Gas Sensor Based on SnO x/SnS Nanostructures with Rich Oxygen Vacancies 2017, 2 1 7.
(7) Keerthana, S.; Rathnakannan, K. Room Temperature Operated Carbon Dioxide Sensor Based on Silver Doped Zinc Oxide/Cupric Oxide Nanoflowers. *Sens. Actuators, B* **2023**, *378*, No. 133181.
(8) Arafat, M. M.; Dinan, B.; Akbar, S. A.; Haseeb, A. S. M. A. Gas Sensors Based on One Dimensional Nanostructured Metal-Oxides: A Review. *Sensors* **2012**, *12* (6), 7207−7258.
(9) Singh, R. P.; Shukla, V. K.; Yadav, R. S.; Sharma, P. K.; Singh, P. K.; Pandey, A. C. Biological Approach of Zinc Oxide Nanoparticles Formation and Its Characterization. *Adv. Mater. Lett.* **2011**, *2* (4), 313−317.
(10) Çolak, H.; Karaköse, E. Synthesis and Characterization of Different Dopant (Ge, Nd, W)-Doped ZnO Nanorods and Their CO2 Gas Sensing Applications. *Sens. Actuators, B* **2019**, *296*, No. 126629.
(11) Ganesh, R. S.; Durgadevi, E.; Navaneethan, M.; Patil, V. L.; Ponnusamy, S.; Muthamizhchelvan, C.; Kawasaki, S.; Patil, P. S.; Hayakawa, Y. Low Temperature Ammonia Gas Sensor Based on Mn-Doped ZnO Nanoparticle Decorated Microspheres. *J. Alloys Compd.* **2017**, *721*, 182−190.
(12) Shao, C.; Chang, Y.; Long, Y. High Performance of Nanostructured ZnO Film Gas Sensor at Room Temperature. *Sens. Actuators, B* **2014**, *204*, 666−672.
(13) Gao, X.; Zhang, T. An Overview: Facet-Dependent Metal Oxide Semiconductor Gas Sensors. *Sens. Actuators, B* **2018**, *277*, 604−633.
(14) Li, G.; Sun, Z.; Zhang, D.; Xu, Q.; Meng, L.; Qin, Y. Mechanism of Sensitivity Enhancement of a ZnO Nanofilm Gas Sensor by UV Light Illumination. *ACS Sens.* **2019**, *4* (6), 1577−1585.
(15) Oskenbay, A.; Salikhov, D.; Rofman, O.; Rakhimbek, I.; Shalabayev, Z.; Khan, N.; Soltabayev, B.; Mentbayeva, A.; Baláž, M.; Tatykayev, B. Solid-State Synthesis of ZnS/ZnO Nanocomposites and Their Decoration with NiS Cocatalyst for Photocatalytic Hydrogen Production. *Ceram. Int.* **2023**, *49* (19), 32246−32260.
(16) Singh, A.; Yadav, B. C. Green Synthesized ZnO/NiO Heterostructures Based Quick Responsive LPG Sensor for the Detection of below LEL with DFT Calculations. *Results Surf. Interfaces* **2023**, *11*, No. 100103.
(17) Ajjaq, A.; Barin, Ö.; Çağırtekin, A.; Soltabayev, B.; Acar, S. ZnO Seed-Mediated Hydrothermal Growth of Advanced 1-D ZnO and 2-D CuO Nanostructured Oxide Ceramics for Gas Sensing Applications. *Ceram. Int.* **2023**, *49*, 40853−40865.
(18) Valerini, D.; Cretì, A.; Caricato, A. P.; Lomascolo, M.; Rella, R.; Martino, M. Optical Gas Sensing through Nanostructured ZnO Films with Different Morphologies. *Sens. Actuators, B* **2010**, *145* (1), 167−173.
(19) Han, J. W.; Rim, T.; Baek, C. K.; Meyyappan, M. Chemical Gated Field Effect Transistor by Hybrid Integration of One-Dimensional Silicon Nanowire and Two-Dimensional Tin Oxide Thin Film for Low Power Gas Sensor. *ACS Appl. Mater. Interfaces* **2015**, *7* (38), 21263−21269.
(20) Wei, S.; Wang, S.; Zhang, Y.; Zhou, M. Different Morphologies of ZnO and Their Ethanol Sensing Property. *Sens. Actuators, B* **2014**, *192*, 480−487.
(21) Franco, M. A.; Conti, P. P.; Andre, R. S.; Correa, D. S. A Review on Chemiresistive ZnO Gas Sensors. *Sens. Actuators Rep.* **2022**, *4*, No. 100100.
(22) Soltabayev, B.; Yergaliuly, G.; Ajjaq, A.; Beldeubayev, A.; Acar, S.; Bakenov, Z.; Mentbayeva, A. Quick NO Gas Sensing by Ti-Doped Flower-Rod-like ZnO Structures Synthesized by the SILAR Method. *ACS Appl. Mater. Interfaces* **2022**, *14* (36), 41555−41570.
(23) Rigi, V. J. C.; Jayaraj, M. K.; Saji, K. J. Envisaging Radio Frequency Magnetron Sputtering as an Efficient Method for Large Scale Deposition of Homogeneous Two Dimensional MoS2. *Appl. Surf. Sci.* **2020**, *529*, No. 147158.
(24) Hosseini, M. R.; Sarvi, M. N. Recent Achievements in the Microbial Synthesis of Semiconductor Metal Sulfide Nanoparticles. *Mater. Sci. Semicond. Process.* **2015**, *40*, 293−301.
(25) Gonçalves, R.; Barrozo, P.; Cunha, F. Optical and Structural Properties of ZnO Thin Films Grown by Magnetron Sputtering: Effect of the Radio Frequency Power. *Thin Solid Films* **2016**, *616*, 265−269.
(26) Luo, Y.; Ly, A.; Lahem, D.; Martin, J. D. M.; Romain, A. C.; Zhang, C.; Debliquy, M. Role of Cobalt in Co-ZnO Nanoflower Gas Sensors for the Detection of Low Concentration of VOCs. *Sens. Actuators, B* **2022**, *360*, No. 131674.
(27) Xu, J. M.; Cheng, J. P. The Advances of Co3O4as Gas Sensing Materials: A Review. *J. Alloys Compd.* **2016**, *686*, 753−768.
(28) Li, Y. J.; Li, K. M.; Wang, C. Y.; Kuo, C. I.; Chen, L. J. Low-Temperature Electrodeposited Co-Doped ZnO Nanorods with Enhanced Ethanol and CO Sensing Properties. *Sens. Actuators, B* **2012**, *161* (1), 734−739.
(29) Hunge, Y. M.; Yadav, A. A.; Kulkarni, S. B.; Mathe, V. L. A Multifunctional ZnO Thin Film Based Devises for Photoelectrocatalytic Degradation of Terephthalic Acid and CO2 Gas Sensing Applications. *Sens. Actuators, B* **2018**, *274*, 1−9.
(30) Wang, D.; Chen, Y.; Liu, Z.; Li, L.; Shi, C.; Qin, H.; Hu, J. CO2-Sensing Properties and Mechanism of Nano-SnO2 Thick-Film Sensor. *Sens. Actuators, B* **2016**, *227*, 73−84.
(31) Singh, A.; Yadav, B. C. Photo-Responsive Highly Sensitive CO2 Gas Sensor Based on SnO2@CdO Heterostructures with DFT Calculations. *Surf. Interfaces* **2022**, *34*, No. 102368.
(32) Chen, G.; Han, B.; Deng, S.; Wang, Y.; Wang, Y. Lanthanum Dioxide Carbonate La2O2CO3 Nanorods as a Sensing Material for Chemoresistive CO2 Gas Sensor. *Electrochim. Acta* **2014**, *127*, 355−361.
(33) Aboud, A. A.; Al-Kelesh, H.; Rouby, W. M. A. E.; Farghali, A. A.; Hamdedein, A.; Khedr, M. H. CO2 Responses Based on Pure and Doped CeO2 Nano-Pellets. *J. Mater. Res. Technol.* **2018**, *7* (1), 14−20.
(34) Karthik, T. V. K.; Martinez, L.; Agarwal, V. Porous Silicon ZnO/SnO2 Structures for CO2 Detection. *J. Alloys Compd.* **2018**, *731*, 853−863.
(35) Hafiz, S. M.; Ritikos, R.; Whitcher, T. J.; Razib, N. M.; Bien, D. C. S.; Chanlek, N.; Nakajima, H.; Saisopa, T.; Songsiriritthigul, P.; Huang, N. M.; Rahman, S. A. A Practical Carbon Dioxide Gas Sensor Using Room-Temperature Hydrogen Plasma Reduced Graphene Oxide. *Sens. Actuators, B* **2014**, *193*, 692−700.
(36) Herrán, J.; Mandayo, G. G.; Castaño, E. Solid State Gas Sensor for Fast Carbon Dioxide Detection. *Sens. Actuators, B* **2008**, *129* (2), 705−709.
(37) Chapelle, A.; El Younsi, I.; Vitale, S.; Thimont, Y.; Nelis, T.; Presmanes, L.; Barnabé, A.; Tailhades, P. Improved Semiconducting CuO/CuFe2O4 Nanostructured Thin Films for CO2 Gas Sensing. *Sens. Actuators, B* **2014**, *204*, 407−413.
(38) Amarnath, M.; Gurunathan, K. Highly Selective CO2 Gas Sensor Using Stabilized NiO-In2O3 Nanospheres Coated Reduced Graphene Oxide Sensing Electrodes at Room Temperature. *J. Alloys Compd.* **2021**, *857*, No. 157584.

https://doi.org/10.1021/acssensors.3c02059
ACS Sens. 2024, 9, 1227−1238

(39) Soltabayev, B.; Ajjaq, A.; Yergaliuly, G.; Kadyrov, Y.; Turlybekuly, A.; Acar, S.; Mentbayeva, A. Ultrasensitive Nitric Oxide Gas Sensors Based on Ti-Doped ZnO Nanofilms Prepared by RF Magnetron Sputtering System. *J. Alloys Compd.* **2023**, *953*, No. 170125.
(40) Nasiri-Tabrizi, B. Thermal Treatment Effect on Structural Features of Mechano-Synthesized Fluorapatite-Titania Nanocomposite: A Comparative Study. *J. Adv. Ceram.* **2014**, *3* (1), 31−42.
(41) Khudiar, A. I.; Khalaf, M. K.; Ofui, A. M. Improvement of the Sensing Characterizations of ZnO Nanostructure by Using Thermal Annealing Prepared through R. F. Magnetron Sputtering Technique. *Opt. Mater.* **2021**, *114*, No. 110885.
(42) Igasaki, Y.; Kanma, H. Argon Gas Pressure Dependence of the Properties of Transparent Conducting ZnO:Al Films Deposited on Glass Substrates. *Appl. Surf. Sci.* **2001**, *169*−*170*, 508−511.
(43) Bindu, P.; Thomas, S. Estimation of Lattice Strain in ZnO Nanoparticles: X-Ray Peak Profile Analysis. *J. Theor. Appl. Phys.* **2014**, *8* (4), 123−134.
(44) Liu, Y.; Luo, W.; Li, R.; Liu, G.; Antonio, M. R.; Chen, X. Optical Spectroscopy of Eu3+ Doped ZnO Nanocrystals. *J. Phys. Chem. C* **2008**, *112* (3), 686−694.
(45) Gandhi, V.; Ganesan, R.; Syedahamed, H. H. A.; Thaiyan, M. Effect of Cobalt Doping on Structural, Optical, and Magnetic Properties of ZnO Nanoparticles Synthesized by Coprecipitation Method. *J. Phys. Chem. C* **2014**, *118* (18), 9717−9725.
(46) Hitkari, G.; Singh, S.; Pandey, G. Photoluminescence Behavior and Visible Light Photocatalytic Activity of ZnO, ZnO/ZnS and ZnO/ZnS/α-Fe2O3 Nanocomposites. *Trans. Nonferrous Met. Soc. China* **2018**, *28* (7), 1386−1396.
(47) Hitkari, G.; Singh, S.; Pandey, G. Structural, Optical and Photocatalytic Study of ZnO and ZnO−ZnS Synthesized by Chemical Method. *Nano-Struct. Nano-Objects* **2017**, *12*, 1−9.
(48) Baiqi, W.; Xudong, S.; Qiang, F.; Iqbal, J.; Yan, L.; Honggang, F.; Dapeng, Y. Photoluminescence Properties of Co-Doped ZnO Nanorods Array Fabricated by the Solution Method. *Phys. E* **2009**, *41* (3), 413−417.
(49) Lin, C. Y.; Wang, W. H.; Lee, C. S.; Sun, K. W.; Suen, Y. W. Magnetophotoluminescence Properties of Co-Doped ZnO Nanorods. *Appl. Phys. Lett.* **2009**, *94* (15), No. 151909.
(50) Taunk, P. B.; Das, R.; Bisen, D. P.; Tamrakar, R. k. Structural Characterization and Photoluminescence Properties of Zinc Oxide Nano Particles Synthesized by Chemical Route Method. *J. Radiat. Res. Appl. Sci.* **2015**, *8* (3), 433−438.
(51) Di Trolio, A.; Bonapasta, A. A.; Barone, C.; Leo, A.; Carapella, G.; Pagano, S.; Polimeni, A.; Testa, A. M. Transport Mechanisms in Co-Doped ZnO (ZCO) and H-Irradiated ZCO Polycrystalline Thin Films. *Phys. Chem. Chem. Phys.* **2021**, *23* (3), 2368−2376.
(52) Di Trolio, A.; Testa, A. M.; Bonapasta, A. A. Ferromagnetic Behavior and Magneto-Optical Properties of Semiconducting Co-Doped ZnO. *Nanomaterials* **2022**, *12* (9), No. 1525.
(53) Maiti, A. SnO 2 Nanoslab as NO 2 Sensor: Identi Fi Cation of the NO 2 Sensing Mechanism on a SnO 2 Surface 2013, 2 2 7.
(54) Moosavi, F.; Bahrololoom, M. E.; Kamjou, R.; Mirzaei, A.; Leonardi, S. G.; Neri, G. Hydrogen Sensing Properties of Co-Doped ZnO Nanoparticles. *Chemosensors* **2018**, *6* (4), No. 61.
(55) Lin, Y.; Fan, Z. Compositing Strategies to Enhance the Performance of Chemiresistive CO2 Gas Sensors. *Mater. Sci. Semicond. Process.* **2020**, *107*, No. 104820.
(56) Fan, Y.; Xu, Y.; Wang, Y.; Sun, Y. Fabrication and Characterization of Co-Doped ZnO Nanodiscs for Selective TEA Sensor Applications with High Response, High Selectivity and Ppb-Level Detection Limit. *J. Alloys Compd.* **2021**, *876*, No. 160170.
(57) Fatima, Z.; Gautam, C.; Singh, A.; Avinashi, S. K.; Yadav, B. C.; Khan, A. A. Synthesis of a Porous SiO2-H3BO3-V2O5-P2O5 Glassy Composite: Structural and Surface Morphological Behaviour for CO2 Gas Sensing Applications. *RSC Adv.* **2022**, *12* (49), 31585−31595.
(58) Goel, N.; Kunal, K.; Kushwaha, A.; Kumar, M. Metal Oxide Semiconductors for Gas Sensing. *Eng. Rep.* **2023**, *5* (6), No. e12604.
(59) Xiong, Y.; Xue, Q.; Ling, C.; Lu, W.; Ding, D.; Zhu, L.; Li, X. Effective CO2 Detection Based on LaOCl-Doped SnO2 Nanofibers: Insight into the Role of Oxygen in Carrier Gas. *Sens. Actuators, B* **2017**, *241*, 725−734.
(60) Tian, X.; Wang, S.; Li, H.; Li, M.; Chen, T.; Xiao, X.; Wang, Y. Recent Advances in MoS2-Based Nanomaterial Sensors for Room-Temperature Gas Detection: A Review. *Sens. Diagn.* **2023**, *2* (2), 361−381.
(61) Mani, G. K.; Rayappan, J. B. B. ZnO Nanoarchitectures: Ultrahigh Sensitive Room Temperature Acetaldehyde Sensor. *Sens. Actuators, B* **2016**, *223*, 343−351.
(62) Godavarti, U.; Mote, V. D.; Reddy, M. V. R.; Nagaraju, P.; Kumar, Y. V.; Dasari, K. T.; Dasari, M. P. Precipitated Cobalt Doped ZnO Nanoparticles with Enhanced Low Temperature Xylene Sensing Properties. *Phys. B* **2019**, *553*, 151−160.
(63) Chu, Y.-L.; Young, S.-J.; Ji, L.-W.; Chu, T.-T.; Lam, K.-T.; Hsiao, Y.-J.; Tang, I.-T.; Kuo, T.-H. Characteristics of Gas Sensors Based on Co-Doped ZnO Nanorod Arrays. *J. Electrochem. Soc.* **2020**, *167* (11), No. 117503.
(64) Zou, C.; Liang, F.; Xue, S. Synthesis and Oxygen Vacancy Related NO 2 Gas Sensing Properties of ZnO:Co Nanorods Arrays Gown by a Hydrothermal Method. *Appl. Surf. Sci.* **2015**, *353* (2), 1061−1069.
(65) Liu, L.; Li, S.; Zhuang, J.; Wang, L.; Zhang, J.; Li, H.; Liu, Z.; Han, Y.; Jiang, X.; Zhang, P. Improved Selective Acetone Sensing Properties of Co-Doped ZnO Nanofibers by Electrospinning. *Sens. Actuators, B* **2011**, *155* (2), 782−788.
(66) Rodrigues, J.; Shimpi, N. G. Detection of Trimethylamine (TMA) Gas Using Mixed Shape Cobalt Doped ZnO Nanostructure. *Mater. Chem. Phys.* **2023**, *305*, No. 127972.
(67) Bhati, V. S.; Ranwa, S.; Kumar, M. In *Highly Sensitive H_2 Gas Sensor of Co Doped ZnO Nanostructures*, AIP Conference Proceedings; AIP, 2018.

https://doi.org/10.1021/acssensors.3c02059
ACS Sens. 2024, 9, 1227−1238